



Published in final edited form as:

Nature. 2017 January 12; 541(7636): 242–246. doi:10.1038/nature20599.

Structures of riboswitch RNA reaction states by mix-and-inject XFEL serial crystallography

J. R. Stagno¹, Y. Liu¹, Y. R. Bhandari¹, C. E. Conrad^{2,3}, S. Panja⁴, M. Swain¹, L. Fan⁵, G. Nelson⁶, C. Li⁶, D. R. Wendel¹, T. A. White⁷, J. D. Coe^{2,3}, M. O. Wiedorn^{7,8}, J. Knoska^{7,8}, D. Oberthuer⁷, R. A. Tuckey¹, P. Yu¹, M. Dyba¹, S. G. Tarasov¹, U. Weierstall^{3,6}, T. D. Grant⁹, C. D. Schwieters¹⁰, J. Zhang¹¹, A. R. Ferré-D'Amaré¹², P. Fromme^{2,3}, D. E. Draper¹³, M. Liang¹⁴, M. S. Hunter¹⁴, S. Boutet¹⁴, K. Tan¹⁵, X. Zuo¹⁶, X. Ji¹⁷, A. Barty⁷, N. A. Zatsepin^{3,6}, H. N. Chapman^{7,8}, J. C. H. Spence^{3,6}, S. A. Woodson⁴, and Y.-X. Wang¹

¹Protein-Nucleic Acid Interaction Section, Structural Biophysics Laboratory, Center for Cancer Research, National Cancer Institute, Frederick, Maryland 21702, USA

²Department of Biochemistry, Arizona State University, Tempe, Arizona 85287, USA

³Center for Applied Structural Discovery, The Biodesign Institute, Arizona State University, Tempe, Arizona 85287, USA

⁴Department of Biophysics, Johns Hopkins University, Baltimore, Maryland 21218, USA

⁵Small Angle X-ray Scattering Core Facility, Center for Cancer Research, National Cancer Institute, Frederick, Maryland 21702, USA

⁶Department of Physics, Arizona State University, Tempe, Arizona 85287, USA

⁷Center for Free-Electron Laser Science, Deutsches Elektronen-Synchrotron DESY, Notkestraße 85, 22607 Hamburg, Germany

⁸Department of Physics, University of Hamburg, Luruper Chaussee 149, 22607 Hamburg, Germany

⁹Hauptmann-Woodward Medical Research Institute, Buffalo, New York 14203, USA

Reprints and permissions information is available at www.nature.com/reprints.

Correspondence and requests for materials should be addressed to Y.-X.W. (wangyunx@mail.nih.gov).

Online Content Methods, along with any additional Extended Data display items and Source Data, are available in the [online version of the paper](#); references unique to these sections appear only in the online paper.

Supplementary Information is available in the [online version of the paper](#).

Author Contributions J.R.S. and Y.-X.W. designed experiments; Y.L. and P.Y. provided the RNA samples; J.R.S. and Y.L. crystallized the RNA; J.R.S., Y.L., Y.R.B., D.R.W., C.E.C., J.D.C., G.N., C.L., N.A.Z., M.O.W., D.O., J.K., T.D.G., M.S.H., S.B., M.L. and Y.-X.W. collected the SFX data; M.O.W., D.O., J.K. and H.N.C. designed the mixing setup; J.R.S., Y.R.B., D.R.W., T.A.W., A.B., R.A.T., N.A.Z., X.J. and T.D.G. processed and analysed the SFX data; J.R.S., Y.R.B., M.S., X.J. and Y.-X.W. interpreted the SFX data; N.A.Z., A.B., M.S.H., S.B., M.L., U.W., P.F., H.N.C. and J.C.H.S. contributed the XFEL expertise and support; Y.R.B., L.F., X.Z., C.D.S. and Y.-X.W. collected, analysed and interpreted SAXS data; J.R.S., C.E.C., K.T. and Y.-X.W. characterized samples; M.D. and Y.L. performed mass spectroscopy; S.G.T. and Y.L. performed ITC and fluorescence titration; S.P. and Y.L. collected and analysed binding data; X.Z. and S.A.W. modelled ligand binding kinetics; X.Z., S.P., S.A.W. and Y.-X.W. interpreted kinetic data; D.E.D., A.F.D. and J.Z. contributed discussions; J.R.S. and Y.-X.W. drafted the manuscript and all authors contributed to the revision.

The authors declare no competing financial interests.

¹⁰Center for Information Technology, National Institutes of Health, Bethesda, Maryland 20892-5624, USA

¹¹Laboratory of Molecular Biology, National Institute of Diabetes and Digestive and Kidney Diseases, National Institutes of Health, Bethesda, Maryland 20892, USA

¹²Laboratory of RNA Biophysics and Cellular Physiology, National Heart Lung and Blood Institute, National Institutes of Health, Bethesda, Maryland 20892, USA

¹³Department of Chemistry, Johns Hopkins University, Baltimore, Maryland 21218, USA

¹⁴Linac Coherent Light Source, SLAC National Accelerator Laboratory, Menlo Park, California 94025, USA

¹⁵Structural Biology Center, Biosciences Division, Advanced Photon Source, Argonne National Laboratory, Argonne, Illinois 60439, USA

¹⁶X-ray Science Division, Advanced Photon Source, Argonne National Laboratory, Argonne, Illinois 60439, USA

¹⁷Macromolecular Crystallography Laboratory, Center for Cancer Research, National Cancer Institute, Frederick, Maryland 21702, USA

Abstract

Riboswitches are structural RNA elements that are generally located in the 5' untranslated region of messenger RNA. During regulation of gene expression, ligand binding to the aptamer domain of a riboswitch triggers a signal to the downstream expression platform¹⁻³. A complete understanding of the structural basis of this mechanism requires the ability to study structural changes over time⁴. Here we use femtosecond X-ray free electron laser (XFEL) pulses^{5,6} to obtain structural measurements from crystals so small that diffusion of a ligand can be timed to initiate a reaction before diffraction. We demonstrate this approach by determining four structures of the adenine riboswitch aptamer domain during the course of a reaction, involving two unbound apo structures, one ligand-bound intermediate, and the final ligand-bound conformation. These structures support a reaction mechanism model with at least four states and illustrate the structural basis of signal transmission. The three-way junction and the P1 switch helix of the two apo conformers are notably different from those in the ligand-bound conformation. Our time-resolved crystallographic measurements with a 10-second delay captured the structure of an intermediate with changes in the binding pocket that accommodate the ligand. With at least a 10-minute delay, the RNA molecules were fully converted to the ligand-bound state, in which the substantial conformational changes resulted in conversion of the space group. Such notable changes *in crystallo* highlight the important opportunities that micro- and nanocrystals may offer in these and similar time-resolved diffraction studies. Together, these results demonstrate the potential of 'mix-and-inject' time-resolved serial crystallography to study biochemically important interactions between biomacromolecules and ligands, including those that involve large conformational changes.

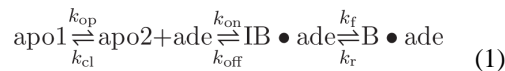
The *add* adenine riboswitch is a translational control riboswitch from *Vibrio vulnificus*⁷. Its aptamer domain is a 71-nucleotide RNA (rA71). The term riboswitch refers to the distinct

conformational switching that takes place in a ligand-sensing aptamer domain after ligand binding, resulting in an altered pattern of gene expression^{2,8}. At the core of the mechanism is a switching sequence^{9–11}, which forms the 3' half of the first helix (P1) of the aptamer domain. We first determined the structures of apo-rA71 using serial femtosecond crystallography (SFX) and micro/nanocrystals (Extended Data Fig. 1), revealing two molecules with distinct conformations (apo1 and apo2) in the asymmetric unit (Fig. 1). The two structures probably represent snapshots of the conformational ensemble present in solution (Extended Data Fig. 2), of which only one (apo2) is ligand-binding competent. Both apo conformers exhibit an overall purine riboswitch architecture^{7,12}, in which helices P2 and P3 are fully formed and the L2–L3 kissing loop interaction is present. However, they differ notably from the ligand-bound form (Protein Data Bank (PDB) accession 4TZX; ref 13) in the three-way junction (Figs 1 and 2a, b) and in P1 (Fig. 1), with the heavy-atom root mean square deviation (r.m.s.d.) values of more than 6 Å for the three-way junctions, and 6.5 Å and 10.3 Å for P1 of apo2 and apo1, respectively (Extended Data Table 2).

The binding pocket was suggested to be locally disordered in the absence of ligand¹⁴. Our structures show that the empty binding pocket is structured. Both apo conformers reveal new sets of hydrogen-bonding and stacking interactions involving key residues (Fig. 2a, b). Consistent with solution studies (Supplementary Discussion)^{14,15}, U48, which is solvent-exposed in the ligand-bound form, flips in to form a wobble base pair either with U75 in apo1, or with the ligand-recognition residue U74 in apo2 (Fig. 2a, b). In particular, the U48•U75 (apo1) and U48•U74 (apo2) interactions are reminiscent of a mutant adenine riboswitch¹⁶. In addition, the role of U48 is similar to that of A14 in the preQ1 riboswitch, both of which rotate into the binding pocket in the absence of ligand¹⁷. In the J2/3 latch region, G46, U47 and U49 form Watson–Crick base pairs with C53, A52 and A73, respectively, and C50 is stacked onto the U47–A52 base pair in both conformers. The J1/2 hinge region exhibits marked differences among all three structures, with r.m.s.d. values of approximately 7.8 Å (apo1 versus bound), 5.9 Å (apo2 versus bound), and 7.2 Å (apo1 versus apo2) (Extended Data Table 2). These differences arise from altered base interactions of U22 and A23 (Fig. 2a, b). In apo2, both U22 and A23 flip out. In apo1, only U22 flips out, forming a hydrogen bond with the backbone of U25 in P2, whereas A23 forms a Hoogsteen base pair with U74, and is wedged between the bases of U48 and U49 (Fig. 2a, b). Both apo structures lack base-triple A73•(A52–U22), as well as the three base-triples, U49•(U20–A76), C50•(U75–A21) and U51•(adenine–U74)•U47 that lock P1 and J2/3 together in the bound structure⁷ (Fig. 2a).

In the absence of ligand-directed coaxial stacking between P1 and P3, the J1/2 hinge serves as a point of rotation for P1. The angular differences in the helical axis of P1 in the apo structures relative to the ligand-bound form are roughly 22° (apo2) and 15° (apo1) (Fig. 1). The rotation and ‘kinking’ at the hinge region in apo1 results in an approximately 8 Å translation of P1 relative to the bound structure (Fig. 1b), and a compression of the major groove formed by helices P1 and P3 in both apo conformers, which is around 10 Å wide compared to more than 16 Å for the ligand-bound conformer (Extended Data Fig. 3b). These changes are the direct results of (1) the loss of the ligand-facilitated coaxial stacking between P1 and P3, in which junction J1/2 acts as a flexible hinge about which P1 pivots, and (2) the loss of key interactions that lock P1 and junction J2/3 together.

Our stopped-flow spectroscopy data suggest at least a four-state kinetics model that not only supports two apo conformations, but also predicts an intermediate-bound (IB) state (Fig. 2c, Extended Data Fig. 4, Supplementary Discussion).



in which B denotes the bound state, k_{on} and k_{off} denote the on-rate and off-rate constants, k_{f} and k_{r} denote the forward and reverse rates, and k_{op} and k_{cl} denote the rate constants for structural opening and closing, respectively.

Visualizing reaction intermediates using trapping or time-resolved crystallography has been reported^{4,18–21}. Here, we use ligand mix-and-inject SFX^{22,23} with RNA microcrystals to determine the structures of four reaction states of the adenine riboswitch in real time (Fig. 3a). Micro- and nanocrystals enable rapid diffusion of the substrate²³ and can accommodate large conformational changes of the molecules (leading to large changes in crystal volume) without breaking the crystal, while the serial measurement approach of measuring a crystal only once is applicable to the study of both reversible and irreversible reactions. The feasibility of mix-and-inject SFX hinges on at least three factors. First, the time of ligand diffusion throughout any given crystal must be negligible compared to that required for conformational changes associated with a reaction in crystals. The linkage time between dynamics and activities of most enzymes and RNA is on the millisecond timescale^{24,25}, whereas diffusion into crystals smaller than about a 10 μm^3 volume is on the sub-millisecond timescale²³. Second, diffusion must be sufficiently uniform so as to minimize crystal strain without destroying crystals during the process of transition. This is achieved because of a much larger surface to volume ratio and a much smaller total volume of a micro/nanocrystal compared to a macroscopic crystal. Third, mixing and delivery of a sample to an XFEL beam must be accomplished sufficiently faster than the rate of conversion to capture conformational intermediates, which can be achieved with a suitable nozzle²².

We first performed mix-and-inject SFX with a long mixing delay of more than 10 min (10-min-mix) to demonstrate the feasibility of converting the RNA *in crystallo* to the final ligand-bound reaction state via relatively large conformation changes (Fig. 1). Both apo1 and apo2 conformers were fully converted to the ligand-bound state, resulting in a polymorphic phase transition to a different space group and unit cell parameters that matched a previously reported structure¹³ (Fig. 3b, c, Extended Data Fig. 5b, c, Methods, Extended Data Table 1). Such a transition may suggest that, in cases where Bragg diffraction is still observable after conversion, rA71 molecules have undergone ‘sufficiently ordered’ structural changes *in crystallo* that enabled the formation of a new lattice. This might be otherwise impossible in macroscopic crystals. It is noteworthy to point out that reactions involving proteins that have been studied thus far using time-resolved crystallography are those in which the structural changes are not large enough to cause a lattice transition^{4,21,26}.

To capture the structure of the IB state using mix-and-inject SFX, the lifetime of the IB state in crystals must be longer than the mixing and diffusion times. In the case of rA71, the concentration of the IB state is expected to peak within milliseconds to seconds according to the time course derived from solution kinetics (Fig. 2d). However, the peak time for the IB structure depends on the actual ligand concentration in the crystals for this non-first-order reaction as well as the crystal lattice constraint. Given that the motions of both RNA and ligands are restricted in the microfluidic crystal environment, we postulated that the ligand-induced transition might not strictly follow the time course predicted by solution kinetics, and that the conversion rate to the bound (B) state might be on the second timescale, sufficiently slow to accumulate a large enough population of the IB state to be detectable by diffraction using the mixing device currently available (Fig. 3a, Extended Data Fig. 5a, Methods).

We performed mix-and-inject SFX with a 10-s mixing delay (10-s-mix) to determine the structure of the intermediate state. The crystal lattice was unchanged (Extended Data Fig. 5b, c), suggesting that no major conformational changes take place within this time interval, characteristic of the IB state based on our kinetic data (Supplementary Discussion). However, the difference electron density revealed key local conformational changes around the binding pocket (Extended Data Fig. 6). Structure analysis and refinement revealed the adenine in the ligand-binding pocket, accompanied by altered conformations for U48 and A21 in the apo2 state (Fig. 4a, b). These changes were not observed in the binding-incompetent apo1 state (Extended Data Fig. 7c).

In the IB structure, the ligand displaces U48 and is stacked between U48 and U49 (U49-adenine-U48) (Fig. 4b), similar to the A21-U48-U49 stacking in the apo2 conformer before binding (Fig. 4a). This is consistent with the low fluorescence of the IB state and little change in the fluorescence from the apo2 to IB states in our kinetic model (Supplementary Discussion). The movement of U48 in turn displaces A21 (Fig. 4b). The adenine ligand in the binding pocket of the IB structure is partially stabilized by hydrogen bonds and base-stacking similar but not identical to those in the bound state (compare Fig. 4f and 4h), forming hydrogen bonds with O4 and N3 of U74 (Fig. 4f). In the absence of ligand, the ligand-recognizing residue U74 is base-paired with A23 or U48 in the apo1 and apo2 states, respectively (Fig. 4e, g). In the IB state, the stacking among U49, ligand, and U48 is reminiscent of the apo1 state, except that the role of the ligand in IB is fulfilled by A23 in apo1 (Fig. 4c). In the apo1 structure, this base stacking together with a unique U48•(U75-A21) base-triple (Fig. 2a) stabilizes apo1 in a 'pseudo-intermediate' structural state, which may explain why the apo1 state is not the first to convert to the IB state within the crystal lattice. The rest of the IB structure, including P1, is similar to that of the apo2 conformer. This is consistent with our kinetics model that predicts the formation of the IB state before the major conformational change (Supplementary Discussion). Furthermore, like the apo1 and apo2 structures, the IB structure still lacks the three base-triple interactions that stabilize P1 in the bound state⁷, resulting in the partial disorder of P1 relative to the rest of the molecule, as indicated by the incomplete electron density for these residues, especially the 3' strand containing the switching sequence (Fig. 4i), and high average B-factors (Extended Data Table 3). These structural heterogeneities, arising from the instability of P1, are also evident from time-averaged molecular dynamics ensemble refinement²⁷ (Fig. 4).

Our results provide both a kinetics mechanistic model and the structural basis for how the signal of ligand binding is transmitted through P1. The low stability of the P1 helix in the context of a riboswitch is not unique to rA71 (refs 9, 28, 29). Thus, modulation from a marginally stable helix in the ligand-free state to a stable helix in the ligand-bound state may be a common strategy to sensitize RNA structural switching to the presence or absence of cognate ligands. Our structures indicate that this is accomplished by ligand-induced rewiring of base interactions in the binding pocket. Equally important, the use of mix-and-inject SFX to determine these structures highlights the potential impact of this method for structural studies of non-photoactivated biological reactions in real time. Because most of these reactions are on the microsecond-to-millisecond timescale, the ensemble-averaging nature of SFX measurements and the properties of micro- and nanocrystals may offer a new route for studying biological reactions and dynamics. In principle, many enzymatic reactions (more than 5,000)³⁰ can be studied this way. These include many other types of interactions involving proteins or nucleic acids with ligands or substrates, such as those in which a very few conformation species in a reaction are dominant and the signals are discernible. As long as micro/nanocrystals of those biomacromolecules can be obtained, further improvements of both XFELs and mixing devices will lead to real-time crystallographic studies of fundamental importance.

Methods

No statistical methods were used to predetermine sample size. The experiments were not randomized and investigators were not blinded to allocation during experiments and outcome assessment.

Apo-rA71 sample preparation and characterization

Apo-rA71 was generated by *in vitro* transcription using a solid-state-immobilized DNA template³¹ and purified by 12% polyacrylamide gel electrophoresis under denaturing conditions. The RNA was eluted from the gel in buffer containing 50 mM sodium acetate, pH 5.3, 2 mM EDTA, and refolded by heating at 80 °C for 2 min and then incubation at 4 °C overnight. The RNA sample was characterized using high-resolution mass spectrometry. Purified apo-rA71 was buffer-exchanged into RNase-free water, followed by buffer containing 10 mM HEPES, pH 7.5, 100 mM KCl, 0.5 mM EDTA (RNA buffer), and concentrated to 40 g l⁻¹. Apo-rA71 was crystallized using the batch method by mixing in 1.5-ml microcentrifuge tubes equal volumes (25 µl each) of RNA solution and crystallization buffer containing 40 mM sodium cacodylate, pH 6.5, 80 mM KCl, 100 mM MgCl₂, 12 mM spermine tetrahydrochloride, and 65% (v/v) (+/-)-2-methyl-2,4-pentanediol (crystallization buffer), followed by incubation at 19–22 °C. Rectangular plate-like microcrystals formed after 1 day at high crystal density and amongst moderate to heavy precipitate. Crystal length typically ranged from 1–10 µm, most of which were approximately 5 µm, with some as large as 20 µm. Microcrystals were characterized visually by bright-field stereomicroscopy with cross-polarization, as well as by UV-TPEF microscopy and second-order nonlinear imaging of chiral crystals (SONICC). Relative diffraction quality of microcrystals, the resolution of which extended to around 6–8 Å, was assessed by powder diffraction using a synchrotron source (Extended Data Fig. 1).

To minimize sample consumption, a viscous stream using an agarose medium was chosen over the conventional liquid-jet sample delivery for SFX³². In preparing the sample for SFX data collection, 0.5 ml of microcrystal suspension was centrifuged briefly to form a concentrated slurry of microcrystals and precipitate, and the pellet was drawn up into a Hamilton syringe. The agarose medium for viscous injection was prepared by dissolving at 95 °C ultra-low gelling agarose (Sigma) at 9% (w/v) in buffer containing 40 mM sodium cacodylate, pH 6.5, 80 mM KCl, 100 mM MgCl₂, 12 mM spermine tetrahydrochloride, and 37.5% (v/v) (+/-)-2-methyl-2,4-pentanediol. The agarose medium was drawn up into a separate Hamilton syringe and allowed to cool to room temperature, forming a gel. The volumes of RNA crystals and agarose medium were adjusted to a ratio of 1:1.7. The syringes were attached to a syringe coupler³³ and the microcrystals were embedded in the agarose medium by mixing to homogeneity. All syringes, lines, and devices were purged with RNase-free water and dried before contact with sample.

High-resolution mass spectrometry

Mass spectrometry data were acquired on an Agilent 6520 Accurate-Mass Q-TOF LC/MS System (Agilent Technologies, Inc.) equipped with a dual electro-spray source, operated in the negative-ion mode. Separation was performed on Clarity 2.6u Oligo-MS 100 A column (2.1 mm × 100 mm). Mobile phase buffer A consisted of 45 mM hexafluoroisopropanol (HFIP), 3 mM triethylamine (TEA) and 10 μM EDTA in water at pH 7.3. Mobile phase buffer B consisted of 45 mM HFIP, 3 mM TEA and 10 μM EDTA in 90% methanol/water. The analytes were eluted at a flow rate of 0.2 ml min⁻¹ with a 10 to 50% organic gradient exchange over 15 min. The instrument was used in full-scan TOF mode. MS source parameters were set with a capillary voltage of 4 kV, the fragmentor voltage of 200 V and skimmer 65 V. The gas temperature was 350 °C, drying gas flow 10 l min⁻¹ and nebulizer pressure 25 psig. Data were acquired at high resolution (3,200 *m/z*), 4 GHz. TOF-MS mass spectra were recorded across the range 200–3,200 *m/z*. Data acquisition and analysis were performed using MassHunter Workstation Software (version B.07.00). To maintain mass accuracy during the run time, an internal mass calibration sample was infused continuously during the liquid chromatography–mass spectrometry (LC/MS) runs.

Characterization of micro- and nanocrystals by powder diffraction

The relative quality of rA71 microcrystals was assessed by room-temperature powder diffraction at the Advanced Photon Source 19ID beamline (Structural Biology Center, Argonne National Laboratory). An aliquot of microcrystal slurry was pelleted in a MicroRT (MiTeGen) capillary, and mounted on a goniometer base. The impact of capillary material was not characterized and may have contributed to background. The sample was exposed to X-rays with a beam size of 0.1 × 0.1 mm², a flux of 3 × 10¹⁴ photons s⁻¹ mm⁻² (before an attenuation factor of 8), sample rotation of 0.1°, and exposure time of 1 s. Diffraction rings could be seen to a resolution of approximately 8 Å, with individual spots extending to around 6 Å (Extended Data Fig. 1f).

Apo-rA71 SFX data collection and analysis

Data were collected using the Coherent X-ray Imaging (CXI) instrument at the Linac Coherent Light Source at the SLAC National Accelerator Laboratory. A continuous stream

of sample was extruded from a 50 μm capillary into the X-ray interaction region using a viscous injector³⁴ at a flow-rate of around 300 nl min^{-1} . The crystals were exposed to 9.2 keV XFEL pulses, each with a duration of 50 fs, at a repetition rate of 120 Hz. The X-rays were focused to 2–3 μm using beryllium lenses, and the transmission was varied from 22 to 100% to minimize saturation, based on live tracking of Bragg peak intensities. Diffraction snapshots from RNA microcrystals were recorded on a Cornell-SLAC Pixel Array Detector (CSPAD). A total of 823,198 frames were recorded, amounting to approximately 1.9 h of total acquisition time and 3.8 TB of raw data.

Cheetah³⁵ was used to extract diffraction patterns ('hits'), defined as those images containing a minimum of 15 peaks. Key peak-finding parameters included the 'peak-finder 8' algorithm, a minimum pixel intensity of 60 analogue-to-digital units (ADU) and a minimum signal-to-noise of 4.2, which yielded an average hit-rate of 22.4% (184,772 hits). The selected diffraction patterns were indexed by CrystFEL 0.6.0 (refs 36–38) using a combination of XDS, MOSFLM and DirAx. The detector geometry was refined to sub-pixel accuracy using CrystFEL's geoptimiser, and the peaks used for indexing were those output from Cheetah. Preliminary indexing results strongly suggested a primitive monoclinic lattice, whose unit cell parameters were then enforced, with a tolerance of 8% for cell axes and 2% for cell angles, to a subsequent round of indexing. The final indexing yield was 13.2% (24,411 indexed patterns). The intensities were integrated in CrystFEL using peak centering, optimized integration radii, and a fixed reciprocal-space profile radius of 0.02 nm^{-1} , and were merged using the average-based Monte Carlo method. For this particular dataset, we found that scaling or post refinement helped only marginally overall, but worsened the data in the higher resolution shells, as judged by figures of merit, R_{split} and CC^* (ref. 39). The data were truncated⁴⁰ to 2.29 \AA resolution based on the CC^* (0.689) of the highest resolution shell (Extended Data Table 1).

Apo-rA71 sample preparation for mix-and-inject SFX using XFEL

Apo-rA71 RNA for ligand-mixing SFX was generated by *in vitro* transcription from PCR template, and purified by phenol/chloroform extraction and ethanol precipitation. The RNA pellets were resuspended in DEPC-treated H_2O and buffer exchanged into 10 mM HEPES, pH 7.5, 100 mM KCl, 0.5 mM EDTA, and concentrated to 20–40 g l^{-1} using an Amicon Ultra-15 Centrifugal Filter device (Merck Milipore). The RNA was crystallized by mixing equal volumes of 5 g l^{-1} RNA and crystallization buffer and 3% (v/v) of a concentrated crystal seed stock, followed by constant mixing/rotation for 2 h at 19–22 $^{\circ}\text{C}$. The plate-like microcrystals (1–10 μm in length; around 5 μm on average) were harvested by centrifugation at 1,000g and the supernatant was removed. The crystals were then washed three times with stabilization buffer (containing equal volumes of RNA buffer and crystallization buffer) to remove any RNA in solution, and the final crystal pellet was resuspended in a minimal volume of stabilization buffer.

Mix-and-inject SFX data collection and analysis

The diffusion-triggered experiments were first proposed in 2000 by the LCLS Scientific Advisory Committee, in 'First Scientific Experiments for LCLS' (<http://www.slac.stanford.edu/pubs/slacreports/reports03/slac-r-611.pdf>). The scheme of the mixing

device is illustrated in Fig. 3a. The setup included two HPLCs with switchboxes. HPLC1 controlled the delivery of sample (filtered through a 20- μm inline filter) or buffer, and HPLC2 controlled the delivery of adenine ligand or buffer. The HPLC lines fed into a T-junction (mixer), which was connected to a gas-directed virtual nozzle (1.5 m in length with 75 μm inner diameter capillary), to provide mixing delay times of several seconds, depending on flow rates. For the 10-s-mix data, the data were collected at a combined flow rate of 30 $\mu\text{l min}^{-1}$: 15 $\mu\text{l min}^{-1}$ each of sample and ligand (10 mM adenine in stabilization buffer).

To determine the structure of the bound-state rA71 after ligand diffusion and in-crystal conversion, the sample was premixed with an equal volume of the 10 mM adenine buffer, and loaded into the sample reservoir. Data acquisition commenced at approximately 10 min after mixing, and continued for around 30 min with a flow rate of 29 $\mu\text{l min}^{-1}$ mixed sample and 1 $\mu\text{l min}^{-1}$ ligand solution.

The crystals were exposed to approximately 9.5 keV XFEL pulses, each with a duration of roughly 45 fs and a pulse energy of about 10^{11} photons, at a repetition rate of 120 Hz. The X-rays were focused to a spot diameter of about 1 μm using KB mirrors, and the beam was attenuated to minimize saturation, based on live tracking of Bragg peak intensities. For the 10-s-mix data, Cheetah hit-finding parameters included a minimum number of 20 peaks, a minimum pixel intensity of 300 ADU and a minimum signal-to-noise ratio (S/N) of 6. Hit-finding parameters for 10-min-mix data were similar, and included 15 peaks, 300 ADU, and minimum S/N of 7. CrystFEL (version 0.6.2+90ff333) was used for indexing, integration and scaling, with very similar parameters to those used for the apo-rA71 data. Whereas the 10-s-mix crystals were isomorphous with the apo-rA71 crystals, the 10 min mixing of ligand into the crystals converted the molecules to the bound state, which was clearly indicated by a change in the space group and unit cell dimensions to that of a previously reported ligand-bound structure. The hit-rate and indexing rates for the 10-s-mix data were 17.0% and 15.8%, respectively, with 14,038 indexed patterns. The hit-rate and indexing rates for the 10-min-mix data were 4.1% and 3.8%, respectively. The ligand-bound crystals suffered markedly from structure conversion, as indicated by diffraction quality and a very low indexing rate. This, and limited available beam time of 6 h for the entire set of measurements, resulted in a final dataset of only 378 indexed patterns (see Extended Data Table 1).

Structure solution and refinement

After numerous attempts using various search models derived from the ligand-bound form of the adenine riboswitch aptamer domain (PDB code 4TZX), the structure of apo-rA71 was solved by PHASER⁴¹ molecular replacement using a truncated version of 4TZX in which residues 13–18, 43–53 and 78–83 were removed. The 10-s-mix structure was solved by refining the apo-rA71 model against the 10-s-mix data, while conserving the test set of reflections from the apo-rA71 data. $F_o - F_c$ and $F_o - F_o$ difference electron density maps calculated using the apo-rA71 model revealed variation between the two datasets in the form of isolated peaks, most likely corresponding to backbone phosphates, predominantly in the apo2 molecule (Extended Data Figs 6a, 7a). This indicated a mixture of at least two

conformers. The occupancies of U48 and A21 of apo2 were set to 0.5 and refined in the same manner. The $F_o - F_c$ map (Extended Data Fig. 6b) clearly indicated the alternative (IB state) conformation of U48 with a blob of density in the original U48 position corresponding to the adenine ligand. The alternative conformation of A21 was much less pronounced and is partially disordered along with the adjacent hinge residues (U22 and A23). Keeping the occupancy of A21 at 0.5, the structure was refined with U48 omitted. The $F_o - F_c$ map (Extended Data Fig. 6c) again strongly supported the alternative configuration of U48, A21, and density for the adenine ligand. The positions of the ligand, U48, and A21 are reminiscent of the apo1 molecule, in which A23 is in place of the ligand, forming similar stacking and H-bond interactions. The final model for the 10-s-mix data contained adenine ligand and two alternative conformations for both U48 and A21, all with occupancies of 0.5 (Extended Data Fig. 6d).

The 10-min-mix converted bound structure was solved by PHASER⁴² MR using PDB code 4TZX as a search model, and was refined using Refmac5 (ref. 43). Despite such a small SFX dataset (378 indexed patterns), the structure was solved to 3.0 Å resolution with surprisingly good electron density for the entire structure, including the adenine ligand, and the flipped-out U48, a signature of the bound state (Fig. 3c). The structure refinement, however, reflects higher-than-normal R-factors owing to such low multiplicity in the SFX data. All crystal data and refinement statistics are summarized in Extended Data Table 1. Final models were obtained using a combination of ERRASER⁴⁴ for automated model building, manual placement of residues in COOT⁴⁵, and iterative cycles of restrained refinement in PHENIX⁴² and Refmac5 (ref. 43) with TLS (apo and IB only). All figures displaying structural coordinates were generated using PyMOL⁴⁶.

Ensemble refinement calculations

Time-averaged molecular dynamics ensemble refinement was performed using PHENIX^{27,42} (version dev-2447) with default parameters, including 0.8 for the fraction of atoms included in TLS fitting, and a temperature of 300 K with 10 steps in the molecular dynamics simulation. The results for each were an ensemble of 20 models. Ensemble refinement was not used for the final model calculations, but rather as a qualitative assessment to demonstrate the varying structural flexibility of the P1 helix in each of the rA71 structures.

Simulation of the time-course of IB state accumulation *in crystallo*

Assuming only the apo2 state is converted to the IB state in the crystal, the binding reaction in crystals can be approximately described by a three-state model. Changing from the IB state to the final binding state B•ade in the crystal is expected to be slow, with k_f assumed to be 0.01 s^{-1} and $k_r = 0 \text{ s}^{-1}$ (no dissociation); k_{on} and k_{off} to be $0.1 \mu\text{M}^{-1} \text{ s}^{-1}$ and 37 s^{-1} respectively (Supplementary Discussion).



Owing to the slow k_f value, a notable population of IB•ade may accumulate within a certain time window. Given the two time points in which 50% and 100% of RNA are converted at $t = 10$ s and 10 min, respectively, and the initial bulk adenine concentration of approximately 5 mM and initial in-crystal apo2 concentration of 15 mM, the time course of the IB•ade buildup is simulated to rationalize the SFX results (Extended Data Fig. 5a).

SAXS data collection and analysis

The procedure for SAXS data collection, processing and analysis are similar to that previously described⁴⁷ using an in-house program package NCI-SAXS or a program package by Svergun and co-workers (<http://www.embl-hamburg.de/biosaxs/>). These procedures and protocols for data collection and processing are in full conformity with the recently published recommended standards⁴⁸. X-ray scattering measurements were carried out at room temperature at the beamlines 12-ID-B of the Advanced Photon Source, the Argonne National Laboratory. The setups were adjusted to achieve scattering q values of $0.006 < q < 0.72 \text{ \AA}^{-1}$, in which $q = (4\pi/\lambda)\sin\theta$, and 2θ is the scattering angle. Twenty two-dimensional (2D) images were recorded for each buffer or sample solution using a flow cell, with the exposure time of 0.5–1.0 s to minimize radiation damage and obtain good signal-to-noise ratio. No radiation damage was observed as confirmed by the absence of systematic signal changes in sequentially collected X-ray scattering images and also confirmed later by gel electrophoresis. The 2D images were reduced to one-dimensional scattering profiles using the MATLAB software package at the beamlines. Scattering profiles of the RNAs were calculated by subtracting the background buffer contribution from the sample-buffer profile. The experimental radius of gyration (R_g) was calculated from the data at low q values in the range of $qR_g < 1.3$, using the Guinier approximation of $\ln I(q) \approx \ln I(0) - R_g^2 q^2/3$.

The solution X-ray scattering curves (Extended Data Fig. 2) were back-calculated using program SolX^{49,50}, and atomic volume parameters for nucleic acids^{51–53}. The same volume parameters were also used in the ensemble calculations^{54,55}. The difference between the back-calculated curve and the experimental data after $q = 0.2 \text{ \AA}^{-1}$ may arise from the flexibility of the molecule in solution, and imperfect simulations on the solvation layer and ion cloud around the molecule.

SAXS ensemble calculations

The Kratky plots of the experimental SAXS data of the aptamer domain of the adenine riboswitch RNA in both the bound and apo states show asymmetric Bell-shape curves (Extended Data Fig. 2a), characteristic of a folded structure with partial flexibility. As discussed in the main text, the holistic view of the apo-rA71 is that flexibility is most likely associated with the hinge and latch regions, and the P1 helix, whereas the kissing loops together with the top parts of the P2 and P3 are relatively rigid. The detailed procedure for the ensemble calculations was carried out using Xplor-NIH as described previously⁵⁵, with exception that the ensemble weight optimization facility⁵⁶ was used in this work. During the calculations, the P2 and P3 helices were treated as rigid bodies, allowing them to rotate and translate freely during simulated annealing. For the P1 helix, the upper part of the helix, A17-U79, G18-C78, A19-U77, U20-A76 and A21-U75, was set as rigid, whereas the

residues G13, G14, G15, and A16 on the 5' end of P1 were set semi-free, and residues C83, C82, C81 and U80 at the 3' end of P1 were allowed to rotate and translate freely, restrained only by covalent linkage. Such restraints were to reflect the 'uncertainty' and account for the difference in occupancy and B-factors of the residues in P1. The force constant for SAXS was set at 100 kcal mol⁻¹, which was ramped so that the calculation could sample conformation space freely without being trapped in a local minimum. The annealing temperature was set at 1,000 K, which was high enough to enable segments of duplexes to freely translate and rotate, but not so high as to disrupt base pairs in duplex regions.

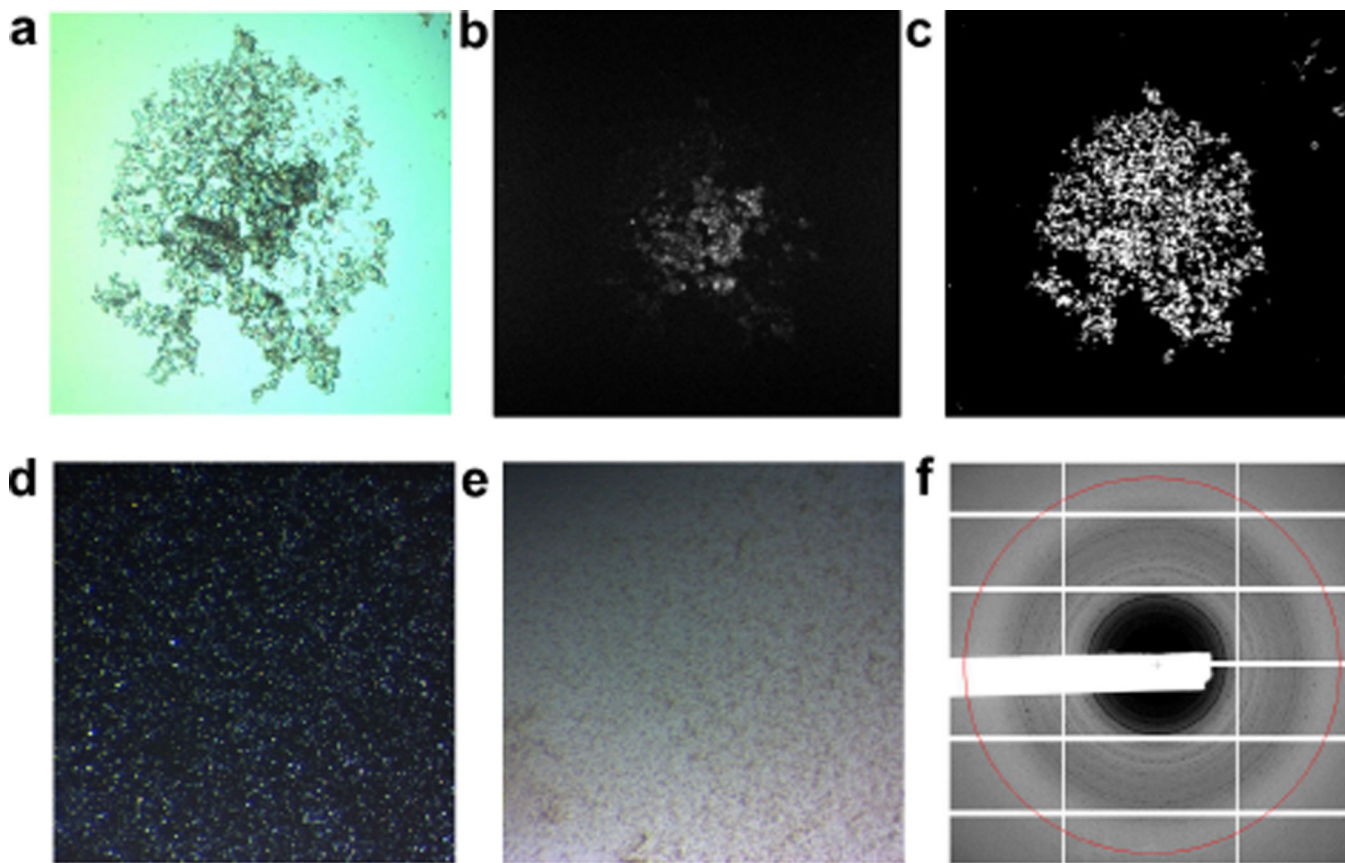
Stopped-flow fluorescence

Riboswitch RNA containing 2-aminopurine (2AP) at position 48 in the ligand-binding pocket (Dharmacon) was gel-purified and deprotected following the manufacturer's protocol. The final material had the expected molecular mass (23,000 D_n) by mass spectrometry. The kinetics of structural changes due to adenine binding in SF buffer (10 mM HEPES, pH 7.5, 100 mM KCl, 10 mM MgCl₂) at 25 °C was measured using an Applied Photophysics SX 18 MV stopped-flow spectrometer. The samples were excited at 318 nm and 2AP fluorescence emission measured using a 335-nm longpass filter. Unless otherwise stated, 0.5 μM 2AP-RNA and 0.5–1,600 μM adenine were mixed with a dead time of 1.8 ms. Six to eight trajectories per sample were averaged and the background intensity was subtracted from each progress curve. The adenine binding kinetics in 5–800 μM adenine was globally fit to the four-state model in equation (1) using MATLAB (MathWorks). See Supplementary Discussion for further details.

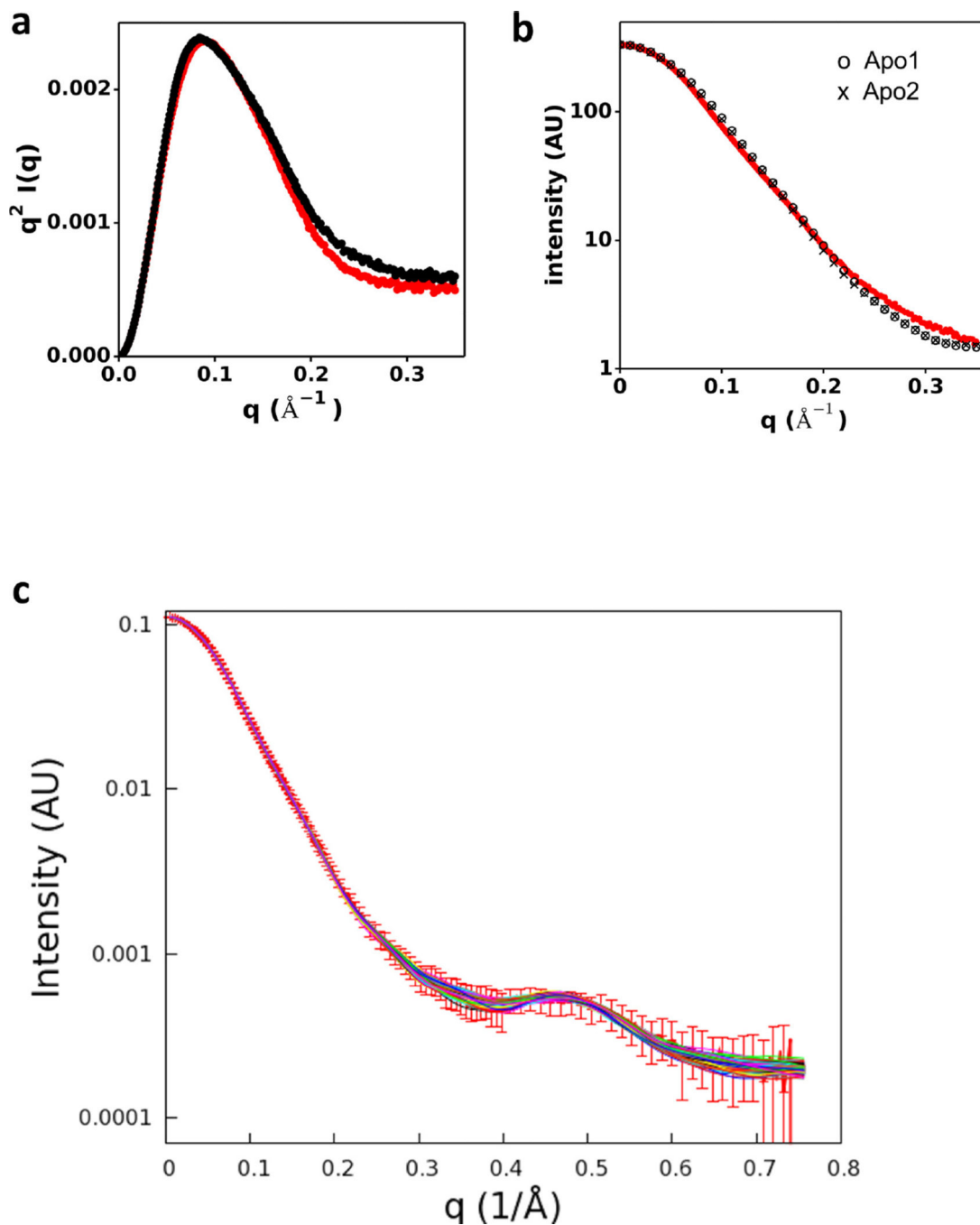
Data availability statement

The atomic coordinates and structure factors have been deposited in the Protein Data Bank (PDB) under accession codes 5E54 (apo-rA71), 5SWD (IB) and 5SWE (B). All other data are available from the corresponding author upon reasonable request.

Extended Data

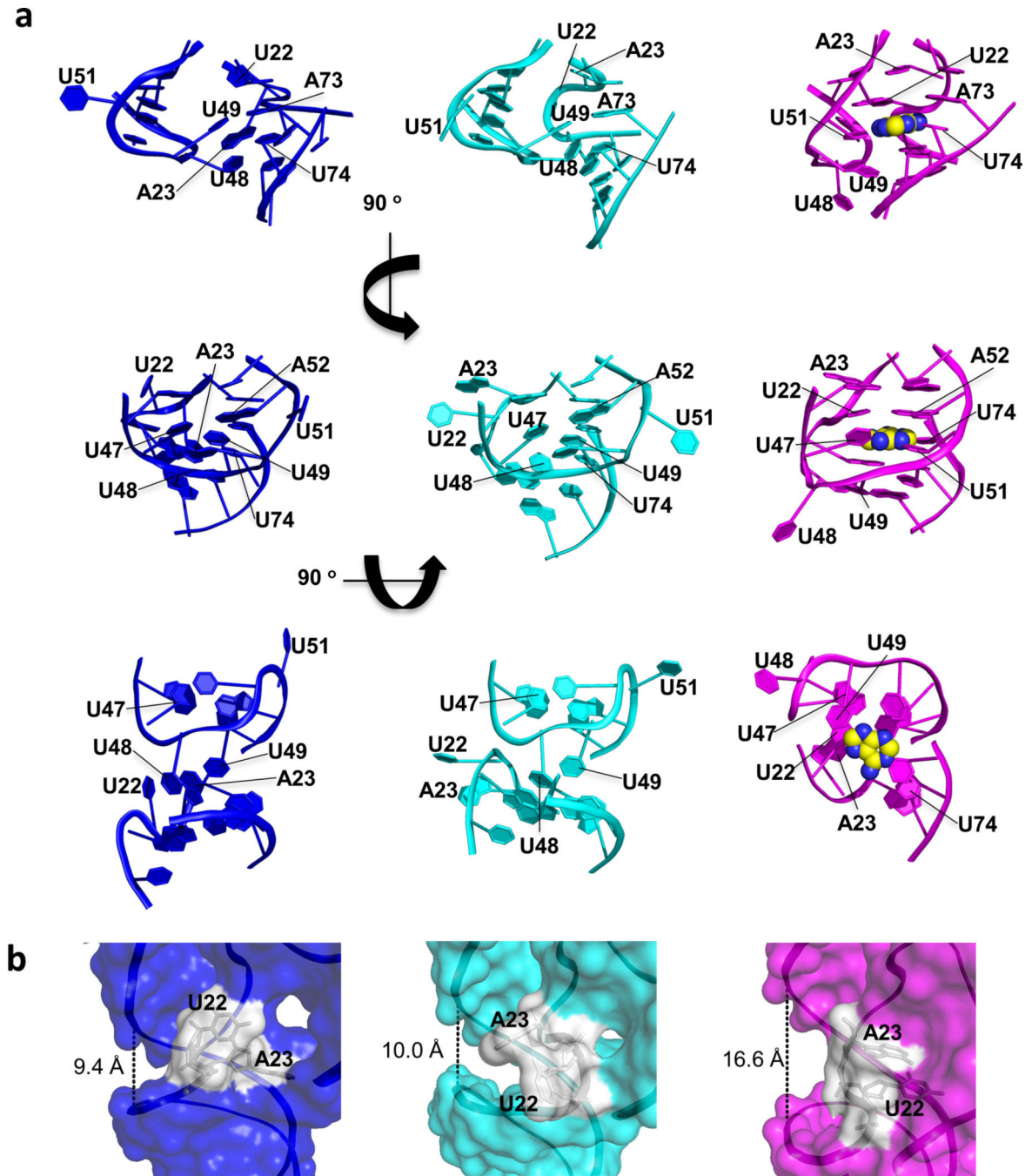
**Extended Data Figure 1. Characterization of RNA crystals**

Microcrystals of apo-rA71 were grown using batch crystallization as described in Methods. A SONICC Imager (Formulatrix) was used to image each sample (0.5–1.0 μl) of crystals using three different methods: visible light (**a**); UV-TPEF (**b**); and second-order nonlinear imaging of chiral crystals (SONICC) (**c**). **d**, Crystal samples were observed using a stereomicroscope (Zeiss) under cross-polarized light. **e**, Without cross-polarization, crystals were barely observable. **f**, The relative quality of the crystalline samples was measured by powder X-ray diffraction (APS beamline 19-ID), with a maximum observable resolution of approximately 6 Å. The resolution ring (red) corresponds to 6.8 Å.



Extended Data Figure 2. Characterization of rA71 in solution by small angle X-ray scattering
a. Comparison of the Kratky plots of the solution X-ray scattering curves of rA71 in the apo (black) and bound (red) states. **b.** Plot of back-calculated small angle X-ray scattering (SAXS) profiles of apo1 and apo2 conformers along with solution X-ray scattering curves of rA71 in the apo (red) states. **c.** Experimental SAXS curve shown in red with red error bars and superimposed with the SAXS curves that were back-calculated from 128 structures using the two-member ensemble calculation. The ratio of the two conformers (apo2:apo1) is

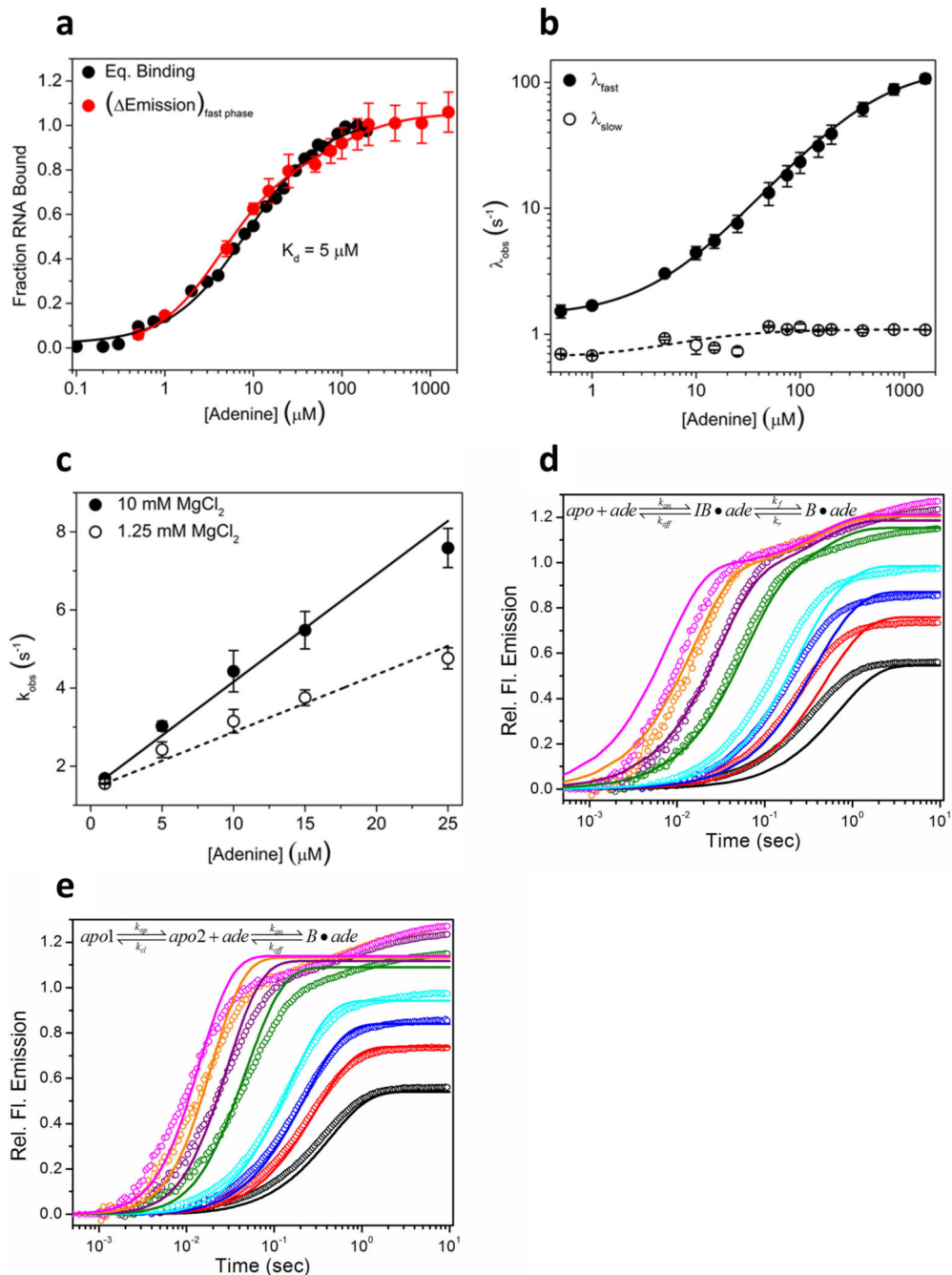
approximately 0.9:0.1 to give the best fit to the experiment data with χ^2 values ranging approximately from 0.1 to 0.3.



Extended Data Figure 3. Three-way junction undergoes notable structural rearrangements to accommodate ligand, compressing the major groove

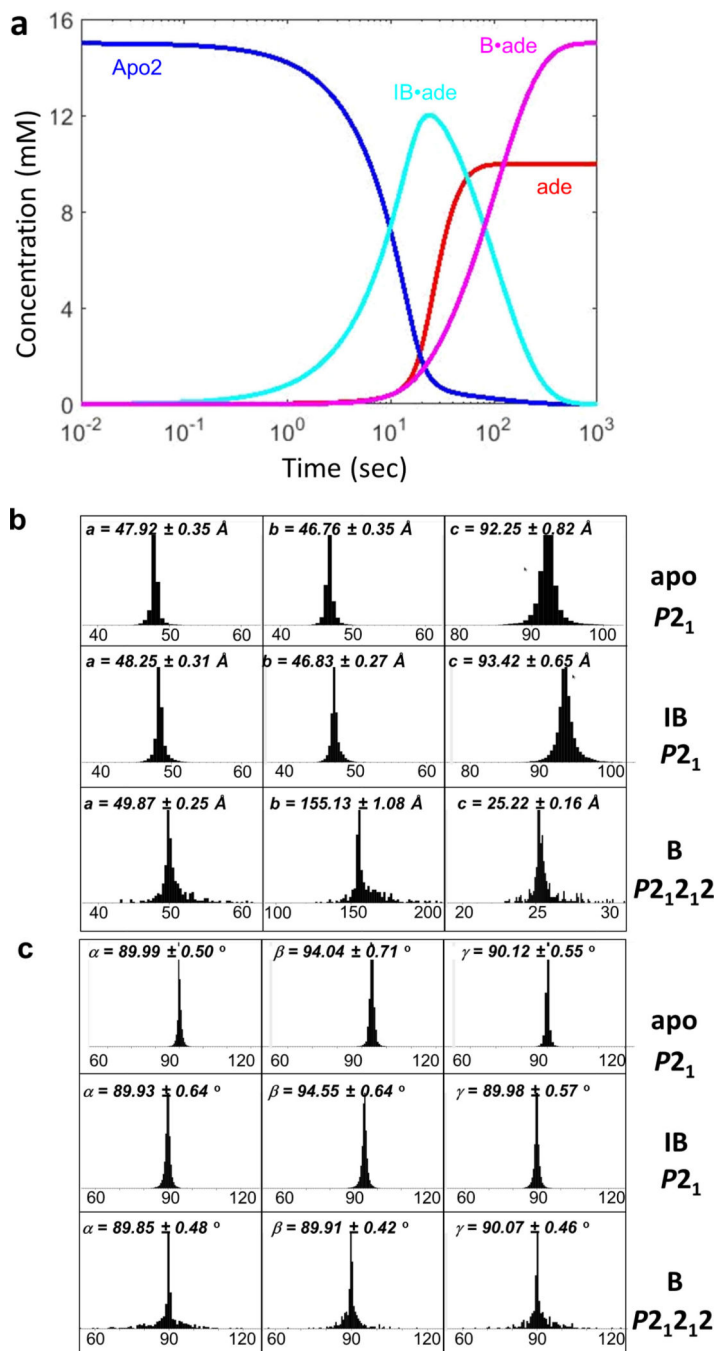
a, The three-way junction, depicted in three orientations, as observed in the apo1 (blue), apo2 (cyan), and ligand-bound (magenta, PDB code 4TZX) structures. Virtually all residues in the three-way junction undergo considerable conformational changes upon ligand binding. Most notable are the ‘swinging’ residues in the hinge (U22, A23) and latch (U48,

U49, U51) regions, the atomic positions of which differ by as much as 17 Å in the apo conformers relative to the ligand-bound conformer. **b**, In the absence of ligand, concerted movement of the hinge (depicted as white surface and stick model) and latch regions results in considerable narrowing of the major groove formed between helices P1 and P3, which measures 9.4 Å, 10.0 Å and 16.6 Å for apo1, apo2 and ligand-bound conformers, respectively. Major groove distances were measured between the phosphorous atoms of U71 and A19 (or U20 in the case of apo1 owing to a difference in register).



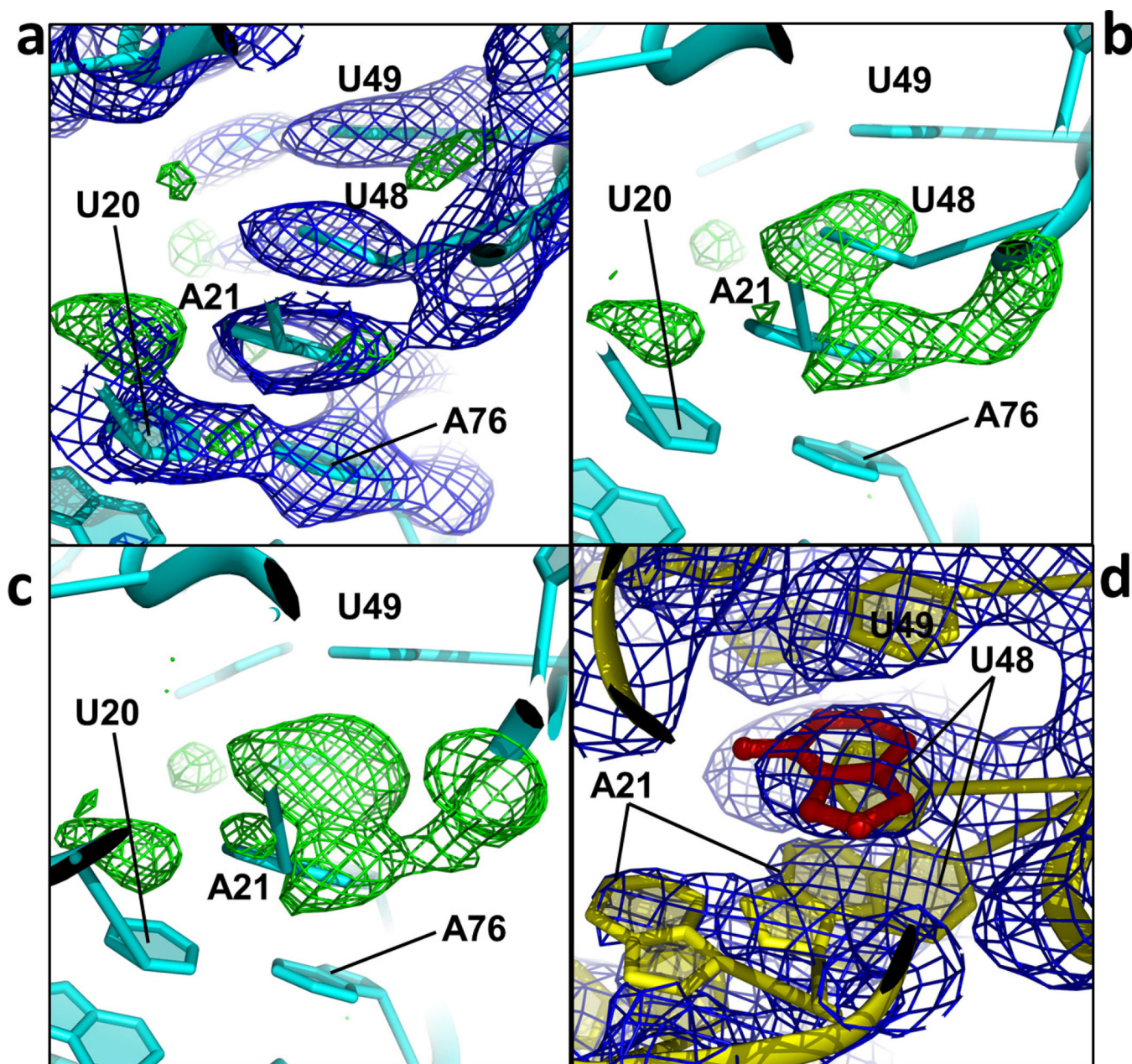
Extended Data Figure 4. Multistage ligand binding kinetics to the rA71 riboswitch

Ligand binding to the rA71 riboswitch was monitored by replacing U48 with the fluorescent base analogue 2-aminopurine (2AP; termed rA71-U482AP). The 2AP fluorescence emission intensity increases upon ligand-induced reorganization of the binding pocket. The 2AP substitution does not change the secondary structure of the apo rA71 riboswitch, as judged by partial RNase digestion. **a**, Equilibrium titration of rA71-U482AP with adenine yields $K_d = 5 \mu\text{M}$ (black symbols). A similar K_d value was obtained from the endpoints of the kinetics progress curves (red symbols) and from in-line probing experiments. This value is about tenfold higher than adenine binding to the unmodified riboswitch, possibly because 2AP forms more stable base-stacking interactions in the apo structure. Error bars show the standard deviation from the average of two or more independent trials. **b**, The ligand-binding kinetics is consistent with a four-state mechanism. Binding of 0.5–1,600 μM adenine to 0.5 μM rA71-U482AP was measured by stopped-flow fluorescence (1.8 ms deadtime), as described in the Methods. The apparent rate constants for adenine association, λ_{fast} and λ_{slow} , were obtained from fits of individual trajectories to a biphasic rate equation, $F = A_{\text{fast}}(1 - \exp(-\lambda_{\text{fast}}t)) + A_{\text{slow}}(1 - \exp(-\lambda_{\text{slow}}t))$, where A denotes for adenine concentrations. Error bars as in **a**. The nonlinear increase in λ_{fast} (filled symbols) with adenine concentration over the full range of ligand concentrations indicates the presence of one or intermediates in the binding mechanism. The ligand-independent phase, λ_{slow} (open symbols), results in biphasic trajectories above 50 μM adenine and is explained by slow exchange between binding competent and binding incompetent forms of the riboswitch. **c**, The apparent bimolecular rate constant for adenine association is slower than diffusion and was obtained from λ_{fast} versus [adenine], under pseudo-first order conditions (0.5–25 μM adenine) in which ligand binding to the competent (open) riboswitch is rate-limiting. In 10 mM MgCl_2 (filled symbols), $k_{\text{on}} = 1.9 \times 10^5 \text{ M}^{-1} \text{ s}^{-1}$ and $k_{\text{off}} = 1.7 \text{ s}^{-1}$. In 1.25 mM MgCl_2 (open symbols), $k_{\text{on}} = 5.2 \times 10^4 \text{ M}^{-1} \text{ s}^{-1}$ and $k_{\text{off}} = 2.1 \text{ s}^{-1}$. The error bars are as in **a** with $n = 3$ over three independent trials. **d, e**, The same set of reduced experimental data in Fig. 2c was globally fit to simpler three-state kinetic mechanisms as described in the Supplementary Discussion. These models were not able to describe the solution binding kinetics over the full-range of ligand concentrations tested. Therefore, the four-state model in equation (1) is the simplest mechanism capable of describing the data. We do not exclude the possibility that the riboswitch samples additional apo states and intermediate complexes that may contribute to the robustness of the switch mechanism. **d**, Three-state mechanism with only one apo state. The parameters obtained from the fitting are: $k_{\text{on}} = 0.28 \mu\text{M}^{-1} \text{ s}^{-1}$, $k_{\text{off}} = 37 \text{ s}^{-1}$, $k_{\text{f}} = 103 \text{ s}^{-1}$, $k_{\text{r}} = 5.1 \text{ s}^{-1}$, $sc = 2.03$. $\text{Err}(k, sc) = 0.053$, where sc is scaling value and rate constants (k) by minimizing a Chi-squared error function $\text{Err}(k, sc)$ that describes the discrepancy between calculated curves and experimental data sets (Supplementary Discussion). **e**, Three-state mechanism with two apo states and no binding intermediate. Parameters: $k_{\text{op}} = 2.5 \text{ s}^{-1}$, $k_{\text{cl}} = 0.58 \text{ s}^{-1}$, $k_{\text{on}} = 0.16 \mu\text{M}^{-1} \text{ s}^{-1}$, $k_{\text{off}} = 0.79 \text{ s}^{-1}$, $sc = 2.44$. $\text{Err}(k, sc) = 0.056$.



Extended Data Figure 5. Time-course simulation of the IB concentration in the crystal and comparison of the unit cell dimensions of the apo, IB and bound structures

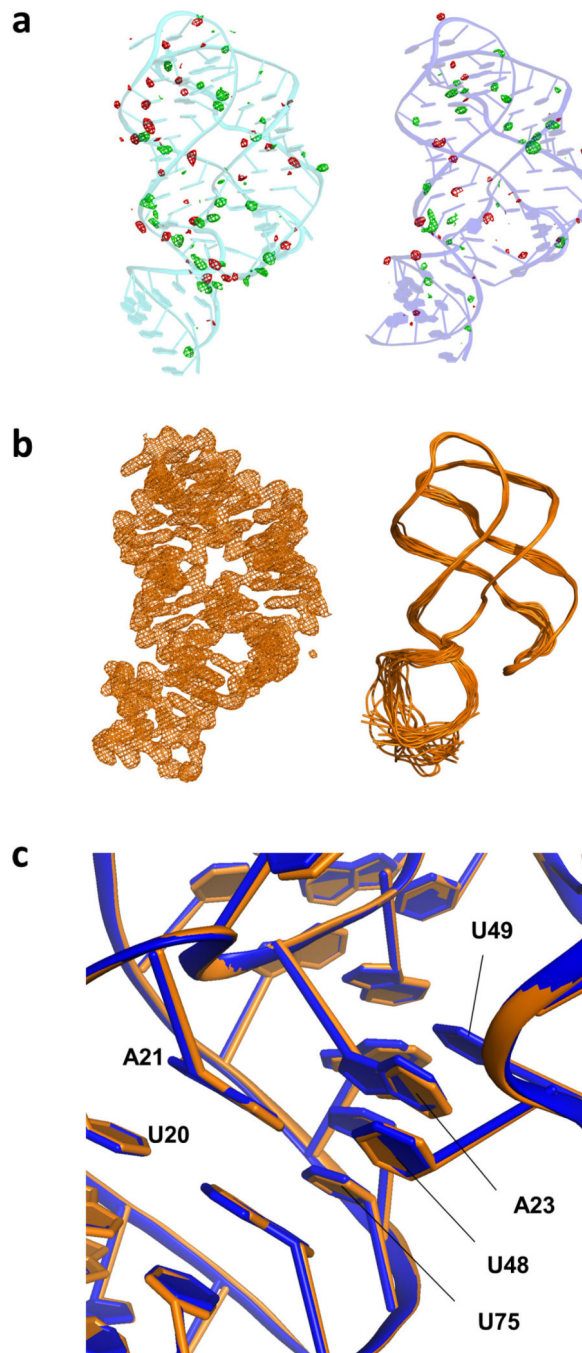
a, Simulated time courses of the IB buildup and changes in concentrations of ligand, apo2 and bound (B) states in the crystal. See also Methods. **b**, **c**, Space group and unit-cell dimensions of the crystals of apo, IB and bound states. The structure was converted in the crystal from the apo to the bound state after at least 10 min of mixing with adenine ligand. The crystal lattice remains unchanged after 10 s of mixing with ligand.



Extended Data Figure 6. Determining the structure of the IB conformer

a, To first verify whether there were changes in the IB state relative to apo2, the apo2 structure was refined against the 10-s-mix data; $2F_o - F_c$ (1σ , blue) and $F_o - F_c$ (3σ , green) electron density maps are shown. Both maps indicated alternative positions for both U48 and A21. **b**, The occupancies of U48 and A21 of the apo2 state were set to 0.5 and refined in the same manner. The $F_o - F_c$ map (3σ , green) clearly indicated the alternative (IB) conformation of U48 with a blob of density in the original U48 position corresponding to the adenine ligand. The alternative conformation of A21 was much less pronounced and is partially disordered along with the adjacent hinge residues (U22 and A23). **c**, Keeping the occupancy of A21 at 0.5, the structure was refined with U48 omitted. The $F_o - F_c$ map (3σ ,

green) again supports the alternative configuration of U48, A21, and density for the adenine ligand. **d**, The final refined structure of the IB state with the adenine ligand (red), and alternative conformations for both U48 and A21 modelled at 0.5 occupancy, shown with $2 F_o - F_c$ electron density map (1σ , blue).



Extended Data Figure 7. $F_o - F_c$ and $2 F_o - F_c$ electron density maps, and ensemble refinement model for the 10-s-mix data

a, Weighted $F_o - F_c$ difference electron density maps in green (3σ) and red (-3σ), computed using the apo structure (apo2, cyan; apo1, blue) and the structure factors from the 10-s-mix

data. The isolated peaks, most likely corresponding to backbone phosphates, indicate a mixture of conformational states, and are predominantly in and around the three-way junction of the apo2 structure. **b**, $2F_o - F_c$ electron density map (1σ , left) and time-averaged molecular dynamics ensemble refinement model (right) for the ‘apo1-like’ molecule of the 10-s-mix structure. **c**, Superimposition of apo1 (blue) and the apo1-like molecule of the 10-s-mix structure (orange), indicating no structural changes to apo1 after 10 s of mixing with ligand.

Extended Data Table 1

Crystal data and refinement statistics

Crystal Data	Apo (5E54) [*]	IB (5SWD)	B (5SWE)
Space group	$P2_1$	$P2_1$	$P2_12_12$
Unit cell parameters			
<i>a</i> , <i>b</i> , <i>c</i> (Å)	47.9, 46.7, 92.3	47.9, 46.7, 92.3	49.9, 154.9, 25.2
<i>b</i> (°)	94.1	94.1	90
Matthews coefficient (Å ³ /Da)	2.33	2.33	2.21
Resolution (Å)	25.02–2.30 (2.38–2.30) [†]	31.06–2.50 (2.59–2.50)	26.32–3.00 (3.31–3.00)
Data acquisition time (min)	114	72	33
Hit rate / Indexing rate (%)	22.4 / 13.2	17.0 / 15.8	4.1 / 3.8
No. indexed patterns	24,411	14,038	378
No. unique reflections	18,368 (1,823)	14,357 (1,431)	4115 (945)
Completeness	1.00 (1.00)	1.00 (1.00)	0.95 (0.87)
R_{split} (%) [‡]	10.92 (81.51)	14.10 (86.84)	66.89 (101.57)
SNR	4.37 (0.27)	3.49 (0.31)	1.37 (0.30)
Multiplicity	461.3 (314.6)	346.8 (188.3)	20.3 (13.0)
$CC^{*§}$	0.998 (0.689)	0.996 (0.462)	0.833 (0.210)
Structure Refinement	Apo (5E54)	IB (5SWD)	B (5SWE)
Resolution range (Å)	25.02–2.30 (2.36–2.30)	30.92–2.50 (2.57–2.50)	26.32–3.00 (3.08–3.00)
No. reflections used	16,995 (972)	13,212 (735)	3,919 (230)
Completeness for range	0.98 (0.79)	0.98 (0.74)	0.95 (0.76)
R_{work}	0.213 (0.640)	0.195 (0.548)	0.349 (0.421)
R_{free}	0.256 (0.660)	0.229 (0.735)	0.379 (0.407)
Wilson B (Å ²)	70.9	80.9	66.4
Average B (Å ²)	77.2	90.6	58.1
No. atoms	2,844	2896	1512
RNA	2,826	2868	1512
Magnesium	4	3	0
Water	14	15	0
Ligand	-	10	10
R.M.S. deviations			
Bond lengths (Å)	0.007	0.007	0.003
Bond angles (°)	1.62	1.52	0.856

Coordinate error (DPI) (Å)	0.24	0.26	0.70
----------------------------	------	------	------

* PDB accession code

† Values in parentheses are for the highest-resolution shell.

$$‡ R_{\text{split}} = \frac{1}{2^{\frac{1}{2}}} \times \frac{\sum_{\text{hkl}} |I_{\text{even}} - I_{\text{odd}}|}{\frac{1}{2} \sum_{\text{hkl}} (I_{\text{even}} + I_{\text{odd}})}$$

$$§ \text{CC}^* = [2\text{CC}_{1/2} / (1 + \text{CC}_{1/2})]^{1/2}$$

$$\parallel R_{\text{work}} = \frac{\sum_{\text{hkl}} ||F_o| - |F_c||}{\sum_{\text{hkl}} |F_o|}, \text{ calculated from the working dataset.}$$

¶ R_{free} is calculated from approximately 5% of data randomly chosen and not included in refinement.

Extended Data Table 2

R.m.s.d. values of all atoms among apo and ligand-bound conformers

Structures aligned with the kissing loops

	3-way jct.	P1 [*]	U48	U51	U74	Hinge	Latch	Kissing loops
apo2 vs. 4TZX	6.4	6.5	13.3	10.1	2.8	5.9	7.5	0.8
apo1 vs. 4TZX	6.2	10.3	11.5	10.0	2.8	7.8	6.8	0.8
apo1 vs. apo2	3.4	6.4	2.8	4.7	1.7	7.2	2.0	0.5
apo1 vs. IB	3.5	5.0	2.3	4.8	1.6	6.4	2.0	0.8
apo2 vs. IB	1.3	1.4	2.4	0.4	0.6	2.5	0.8	0.3
IB vs. 4TZX	5.6	6.6	12.2	9.9	3.2	5.4	6.5	0.89

Whole structure alignments

	3-way jct.	P1 [*]	U48	U51	U74	Hinge	Latch	Kissing loops
apo2 vs. 4TZX	5.6	2.5	10.6	10.0	2.3	1.6	4.9	0.9
apo1 vs. 4TZX	5.6	3.4	7.9	10.6	2.3	1.7	4.8	0.8
apo1 vs. apo2	3.6	1.5	2.6	2.0	1.6	2.4	1.4	0.3
apo1 vs. IB	3.3	3.8	2.3	3.9	1.8	6.2	1.8	1.1
apo2 vs. IB	1.3	1.3	2.4	0.3	0.4	0.3	0.8	0.3
IB vs. 4TZX	5.5	4.1	10.7	10.9	2.4	5.1	6.4	1.4

* The r.m.s.d. values (Å) of P1 when compared alone are among the three structures:

1.3 Å (apo2 versus bound); 0.9 Å (apo1 versus bound); 1.0 Å (apo2 versus apo1); 1.4 Å (IB versus bound); 1.3 Å (IB versus apo1); 1.3 Å (IB versus apo2).

Extended Data Table 3

Average B-factors (Å²)

	Overall	P1 [†]
apo1 (13–77) [*]	76.7	122.9
apo2 (13–80)	77.1	131.0
IB (13–77)	92.7	158.9
IB-apo1 (13–80)	88.1	137.1
bound (13–83)	57.9	69.1

* Numbers in parentheses indicate the range of residues modelled.
 † Residues 13–21 and 75–83.

Supplementary Material

Refer to Web version on PubMed Central for supplementary material.

Acknowledgments

Portions of this research were carried out at the Linac Coherent Light Source, a National User Facility operated by Stanford University on behalf of the US Department of Energy, Office of Basic Energy Sciences. The CXI instrument was funded by the LCLS Ultrafast Science Instruments (LUSI) project funded by the US Department of Energy, Office of Basic Energy Sciences. Use of the Linac Coherent Light Source (LCLS), SLAC National Accelerator Laboratory, is supported by the US Department of Energy, Office of Science, Office of Basic Energy Sciences under Contract No. DE-AC02-76SF00515. We thank J. Strathern and M. Dunne for their support and S. Wakatsuki for discussions. This work is supported in part by the NSF-STC “BioXFEL” (NSF-1231306), the NIH Intramural Research Programs of NCI, CIT, NHLBI, and the US Department of Energy, Office of Biological and Environmental Research under Contract DE-AC02-06CH11357, the European Research Council, “Frontiers in Attosecond X-ray Science: Imaging and Spectroscopy (AXSIS)”, ERC-2013-SyG 609920, and the BMBF through project 05K16GU1.

References

- Mandal M, Boese B, Barrick JE, Winkler WC, Breaker RR. Riboswitches control fundamental biochemical pathways in *Bacillus subtilis* and other bacteria. *Cell*. 2003; 113:577–586. [PubMed: 12787499]
- Nahvi A, et al. Genetic control by a metabolite binding mRNA. *Chem. Biol.* 2002; 9:1043. [PubMed: 12323379]
- Breaker RR. Riboswitches and the RNA world. *Cold Spring Harb. Perspect. Biol.* 2012; 4:a003566. [PubMed: 21106649]
- Hajdu J, et al. Analyzing protein functions in four dimensions. *Nat. Struct. Biol.* 2000; 7:1006–1012. [PubMed: 11062553]
- Boutet S, et al. High-resolution protein structure determination by serial femtosecond crystallography. *Science*. 2012; 337:362–364. [PubMed: 22653729]
- Chapman HN, et al. Femtosecond X-ray protein nanocrystallography. *Nature*. 2011; 470:73–77. [PubMed: 21293373]
- Serganov A, et al. Structural basis for discriminative regulation of gene expression by adenine- and guanine-sensing mRNAs. *Chem. Biol.* 2004; 11:1729–1741. [PubMed: 15610857]
- Winkler WC, Breaker RR. Genetic control by metabolite-binding riboswitches. *ChemBioChem*. 2003; 4:1024–1032. [PubMed: 14523920]
- Batey RT. Structure and mechanism of purine-binding riboswitches. *Q. Rev. Biophys.* 2012; 45:345–381. [PubMed: 22850604]
- Di Palma F, Colizzi F, Bussi G. Ligand-induced stabilization of the aptamer terminal helix in the add adenine riboswitch. *RNA*. 2013; 19:1517–1524. [PubMed: 24051105]
- Lemay JF, Lafontaine DA. The adenine riboswitch: a new gene regulation mechanism. *Med. Sci. (Paris)*. 2006; 22:1053–1059. [PubMed: 17156726]
- Batey RT, Gilbert SD, Montange RK. Structure of a natural guanine-responsive riboswitch complexed with the metabolite hypoxanthine. *Nature*. 2004; 432:411–415. [PubMed: 15549109]
- Zhang J, Ferré-D’Amaré AR. Dramatic improvement of crystals of large RNAs by cation replacement and dehydration. *Structure*. 2014; 22:1363–1371. [PubMed: 25185828]
- Rieder R, Lang K, Graber D, Micura R. Ligand-induced folding of the adenosine deaminase A-riboswitch and implications on riboswitch translational control. *ChemBioChem*. 2007; 8:896–902. [PubMed: 17440909]
- Gilbert SD, Stoddard CD, Wise SJ, Batey RT. Thermodynamic and kinetic characterization of ligand binding to the purine riboswitch aptamer domain. *J. Mol. Biol.* 2006; 359:754–768. [PubMed: 16650860]

16. Delfosse V, et al. Riboswitch structure: an internal residue mimicking the purine ligand. *Nucleic Acids Res.* 2010; 38:2057–2068. [PubMed: 20022916]
17. Jenkins JL, Krucinska J, McCarty RM, Bandarian V, Wedekind JE. Comparison of a preQ1 riboswitch aptamer in metabolite-bound and free states with implications for gene regulation. *J. Biol. Chem.* 2011; 286:24626–24637. [PubMed: 21592962]
18. Pande K, et al. Femtosecond structural dynamics drives the *trans/cis* isomerization in photoactive yellow protein. *Science.* 2016; 352:725–729. [PubMed: 27151871]
19. Tenboer J, et al. Time-resolved serial crystallography captures high-resolution intermediates of photoactive yellow protein. *Science.* 2014; 346:1242–1246. [PubMed: 25477465]
20. Barends TR, et al. Direct observation of ultrafast collective motions in CO myoglobin upon ligand dissociation. *Science.* 2015; 350:445–450. [PubMed: 26359336]
21. Hajdu J, et al. Millisecond X-ray diffraction and the first electron density map from Laue photographs of a protein crystal. *Nature.* 1987; 329:178–181. [PubMed: 3114644]
22. Wang D, Weierstall U, Pollack L, Spence J. Double-focusing mixing jet for XFEL study of chemical kinetics. *J. Synchrotron Radiat.* 2014; 21:1364–1366. [PubMed: 25343806]
23. Schmidt M. Mix and inject: reaction initiation by diffusion for time-resolved acromolecular crystallography. *Adv. Condens. Matter Phys.* 2013; 2013:167276.
24. Wolf-Watz M, et al. Linkage between dynamics and catalysis in a thermophilic-mesophilic enzyme pair. *Nat. Struct. Mol. Biol.* 2004; 11:945–949. [PubMed: 15334070]
25. Al-Hashimi HM, Walter NG. RNA dynamics: it is about time. *Curr. Opin. Struct. Biol.* 2008; 18:321–329. [PubMed: 18547802]
26. Campbell JW, et al. Calcium binding sites in tomato bushy stunt virus visualized by Laue crystallography. *J. Mol. Biol.* 1990; 214:627–632. [PubMed: 2388260]
27. Burnley BT, Afonine PV, Adams PD, Gros P. Modelling dynamics in protein crystal structures by ensemble refinement. *eLife.* 2012; 1:e00311. [PubMed: 23251785]
28. Huang L, Ishibe-Murakami S, Patel DJ, Serganov A. Long-range pseudoknot interactions dictate the regulatory response in the tetrahydrofolate riboswitch. *Proc. Natl Acad. Sci. USA.* 2011; 108:14801–14806. [PubMed: 21873197]
29. Haller A, Altman RB, Soulière MF, Blanchard SC, Micura R. Folding and ligand recognition of the TPP riboswitch aptamer at single-molecule resolution. *Proc. Natl Acad. Sci. USA.* 2013; 110:4188–4193. [PubMed: 23440214]
30. Spence J, Lattman E. Imaging enzyme kinetics at atomic resolution. *IUCrJ.* 2016; 3:228–229.
31. Liu Y, et al. Synthesis and applications of RNAs with position-selective labelling and mosaic composition. *Nature.* 2015; 522:368–372. [PubMed: 25938715]
32. Conrad CE, et al. A novel inert crystal delivery medium for serial femtosecond crystallography. *IUCrJ.* 2015; 2:421–430.
33. Cheng A, Hummel B, Qiu H, Caffrey M. A simple mechanical mixer for small viscous lipid-containing samples. *Chem. Phys. Lipids.* 1998; 95:11–21. [PubMed: 9807807]
34. Weierstall U, et al. Lipidic cubic phase injector facilitates membrane protein serial femtosecond crystallography. *Nat. Commun.* 2014; 5:3309. [PubMed: 24525480]
35. Barty A, et al. *Cheetah*: software for high-throughput reduction and analysis of serial femtosecond X-ray diffraction data. *J. Appl. Crystallogr.* 2014; 47:1118–1131. [PubMed: 24904246]
36. White TA, et al. *CrystFEL*: a software suite for snapshot serial crystallography. *J. Appl. Crystallogr.* 2012; 45:335–341.
37. Kirian RA, et al. Structure-factor analysis of femtosecond microdiffraction patterns from protein nanocrystals. *Acta Crystallogr. A.* 2011; 67:131–140. [PubMed: 21325716]
38. White TA, et al. Crystallographic data processing for free-electron laser sources. *Acta Crystallogr. D.* 2013; 69:1231–1240. [PubMed: 23793149]
39. Karplus PA, Diederichs K. Linking crystallographic model and data quality. *Science.* 2012; 336:1030–1033. [PubMed: 22628654]
40. French GS, Wilson KS. On the treatment of negative intensity observations. *Acta Crystallogr. A.* 1978; 34:517–525.

41. McCoy AJ, et al. Phaser crystallographic software. *J. Appl. Crystallogr.* 2007; 40:658–674. [PubMed: 19461840]
42. Adams PD, et al. PHENIX: building new software for automated crystallographic structure determination. *Acta Crystallogr. D.* 2002; 58:1948–1954. [PubMed: 12393927]
43. Murshudov GN, et al. REFMAC5 for the refinement of macromolecular crystal structures. *Acta Crystallogr. D.* 2011; 67:355–367. [PubMed: 21460454]
44. Chou FC, Sripakdeevong P, Dibrov SM, Hermann T, Das R. Correcting pervasive errors in RNA crystallography through enumerative structure prediction. *Nat. Methods.* 2013; 10:74–76. [PubMed: 23202432]
45. Emsley P, Cowtan K. Coot: model-building tools for molecular graphics. *Acta Crystallogr. D.* 2004; 60:2126–2132. [PubMed: 15572765]
46. The PyMOL Molecular Graphics System, Version 1.7.6.4. Schrödinger: LLC;
47. Wang J, et al. A method for helical RNA global structure determination in solution using small-angle x-ray scattering and NMR measurements. *J. Mol. Biol.* 2009; 393:717–734. [PubMed: 19666030]
48. Jacques DA, Guss JM, Trehwella J. Reliable structural interpretation of small-angle scattering data from bio-molecules in solution—the importance of quality control and a standard reporting framework. *BMC Struct. Biol.* 2012; 12:9. [PubMed: 22595034]
49. Zuo X, et al. X-ray diffraction “fingerprinting” of DNA structure in solution for quantitative evaluation of molecular dynamics simulation. *Proc. Natl Acad. Sci. USA.* 2006; 103:3534–3539. [PubMed: 16505363]
50. Tiede DM, Mardis KL, Zuo X. X-ray scattering combined with coordinate-based analyses for applications in natural and artificial photosynthesis. *Photosynth. Res.* 2009; 102:267–279. [PubMed: 19636808]
51. Zuo X, et al. Global molecular structure and interfaces: refining an RNA:RNA complex structure using solution X-ray scattering data. *J. Am. Chem. Soc.* 2008; 130:3292–3293. [PubMed: 18302388]
52. Nadassy K, Tomás-Oliveira I, Alberts I, Janin J, Wodak SJ. Standard atomic volumes in double-stranded DNA and packing in protein--DNA interfaces. *Nucleic Acids Res.* 2001; 29:3362–3376. [PubMed: 11504874]
53. Voss NR, Gerstein M. Calculation of standard atomic volumes for RNA and comparison with proteins: RNA is packed more tightly. *J. Mol. Biol.* 2005; 346:477–492. [PubMed: 15670598]
54. Schwieters CD, Kuszewski JJ, Tjandra N, Clore GM. The Xplor-NIH NMR molecular structure determination package. *J. Magn. Reson.* 2003; 160:65–73. [PubMed: 12565051]
55. Fang X, et al. An unusual topological structure of the HIV-1 Rev response element. *Cell.* 2013; 155:594–605. [PubMed: 24243017]
56. Deshmukh L, et al. Structure and dynamics of full-length HIV-1 capsid protein in solution. *J. Am. Chem. Soc.* 2013; 135:16133–16147. [PubMed: 24066695]

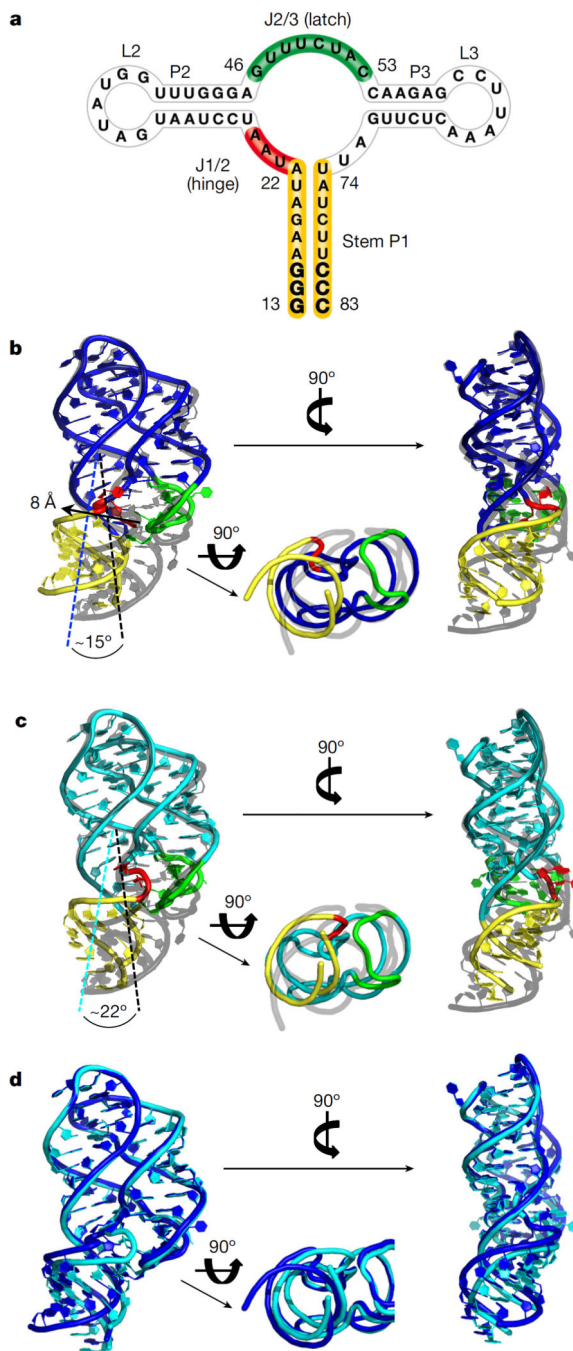


Figure 1. Structure comparison of the ligand-bound and apo conformers
a, Secondary structure of rA71 with key regions highlighted in yellow (P1), red (hinge), and green (latch). The three consecutive GC pairs in P1 are illustrated in bold. **b–d**, Cartoon representations in three different views, with key regions colour-coded as in **a**, comparing the structures of apo1 (blue) and ligand-bound (grey, PDB code 4TZX) (**b**); apo2 (cyan) and ligand-bound (grey) (**c**); and apo1 (blue) and apo2 (cyan) (**d**). The structures were aligned against the kissing-loops (L2 and L3), residues 29–41 and 58–68.

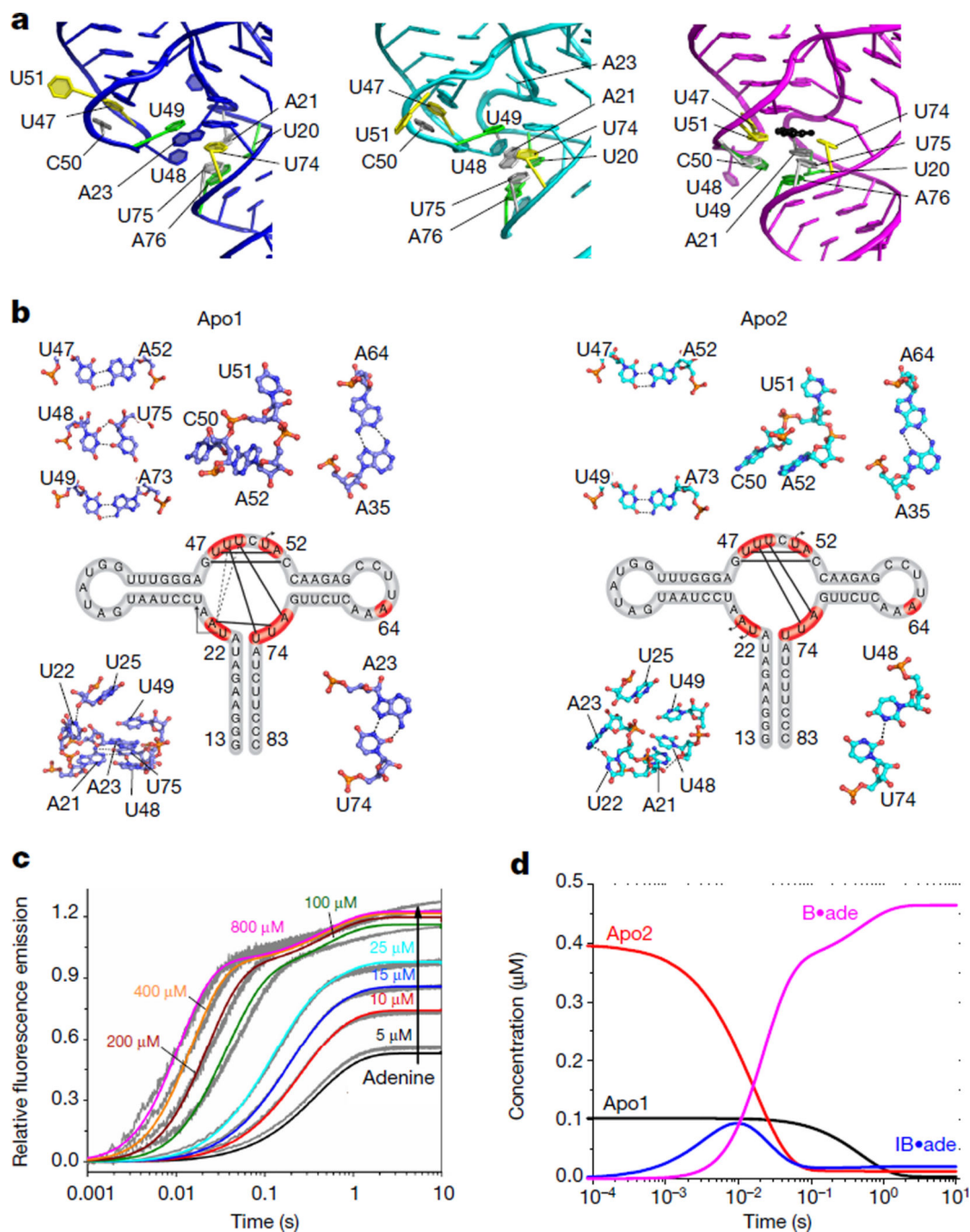


Figure 2. Structures of the three-way junction in the absence of ligand

a, The three-way junction, as observed in apo1 (blue), apo2 (cyan), and ligand-bound (magenta, PDB code 4TZX) structures, with base triples (yellow, grey and green) and adenine ligand (black) indicated. **b**, Secondary structures and detailed interactions (shown as ball-and-stick) of key residues (red) within the junctions of each of the apo conformers. In the secondary structure map, base pairs are depicted as solid black lines, and the movements of residues that flip outward are shown as black arrows. The stacking of A23 between U48 and U49 in apo1 is illustrated as dotted lines. **c**, Trajectories are shown for eight

concentrations of adenine and are globally fit to the model in equation (1) (Supplementary Discussion). **d**, Evolution of species concentrations over time (Supplementary Discussion).

Author Manuscript

Author Manuscript

Author Manuscript

Author Manuscript

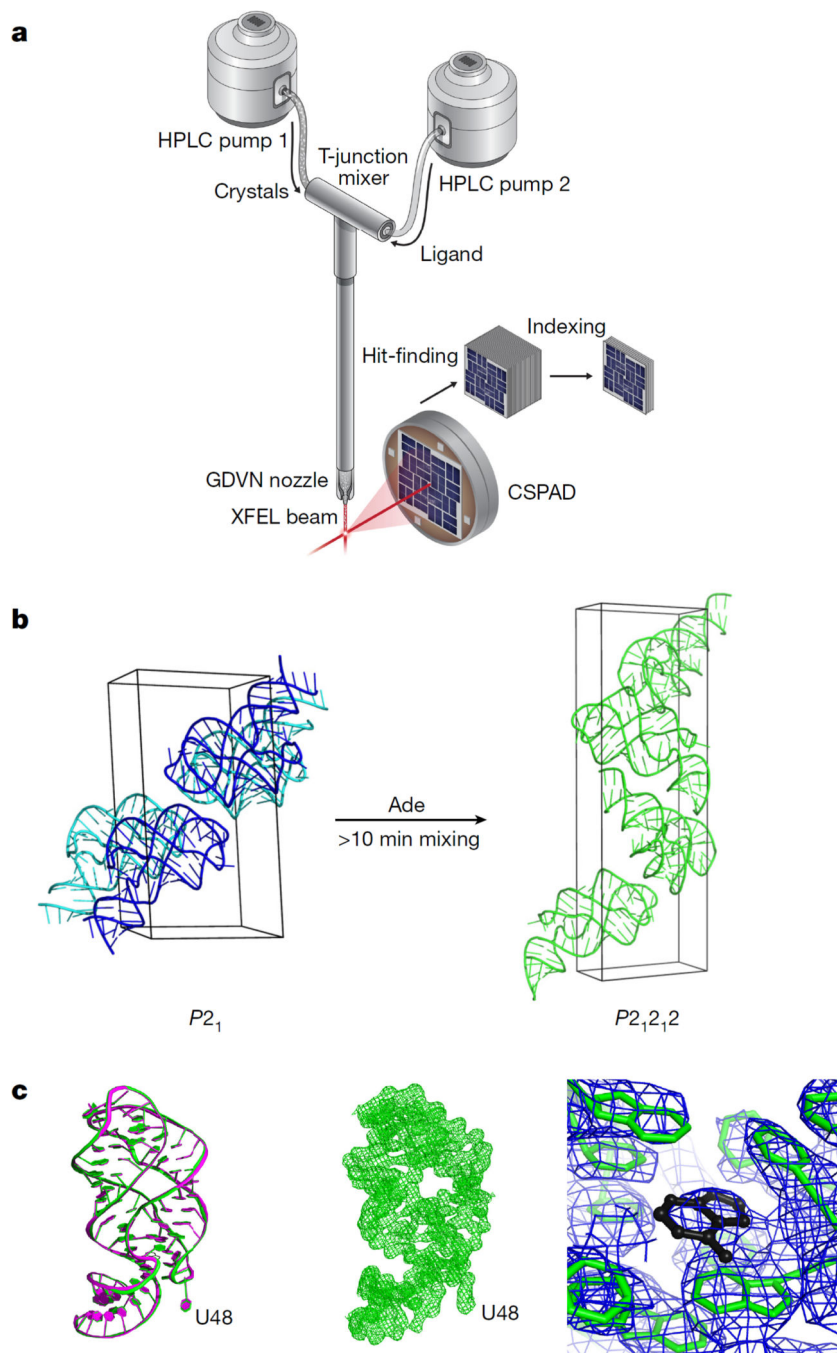


Figure 3. Setup of mix-and-inject SFX and conversion of the structure and crystal lattice
a. Cartoon of the SFX ligand-mixing experiment. For details, see Methods. **b.** The unit cells of the crystals of apo ($P2_1$) and ligand-bound ($P2_12_12$), the structure of which was generated *in crystallo* from the apo structures after at least 10 min of mixing with the adenine ligand (Extended Data Fig. 5b, c). **c.** Superimposition (left) of the ligand-bound structures of the 10-min-mix (green) and PDB code 4TZX (magenta), and $2F_o - F_c$ electron density maps contoured at 1σ for the whole structure of the 10-min-mix (middle) and the binding pocket (right) showing the ligand (black).

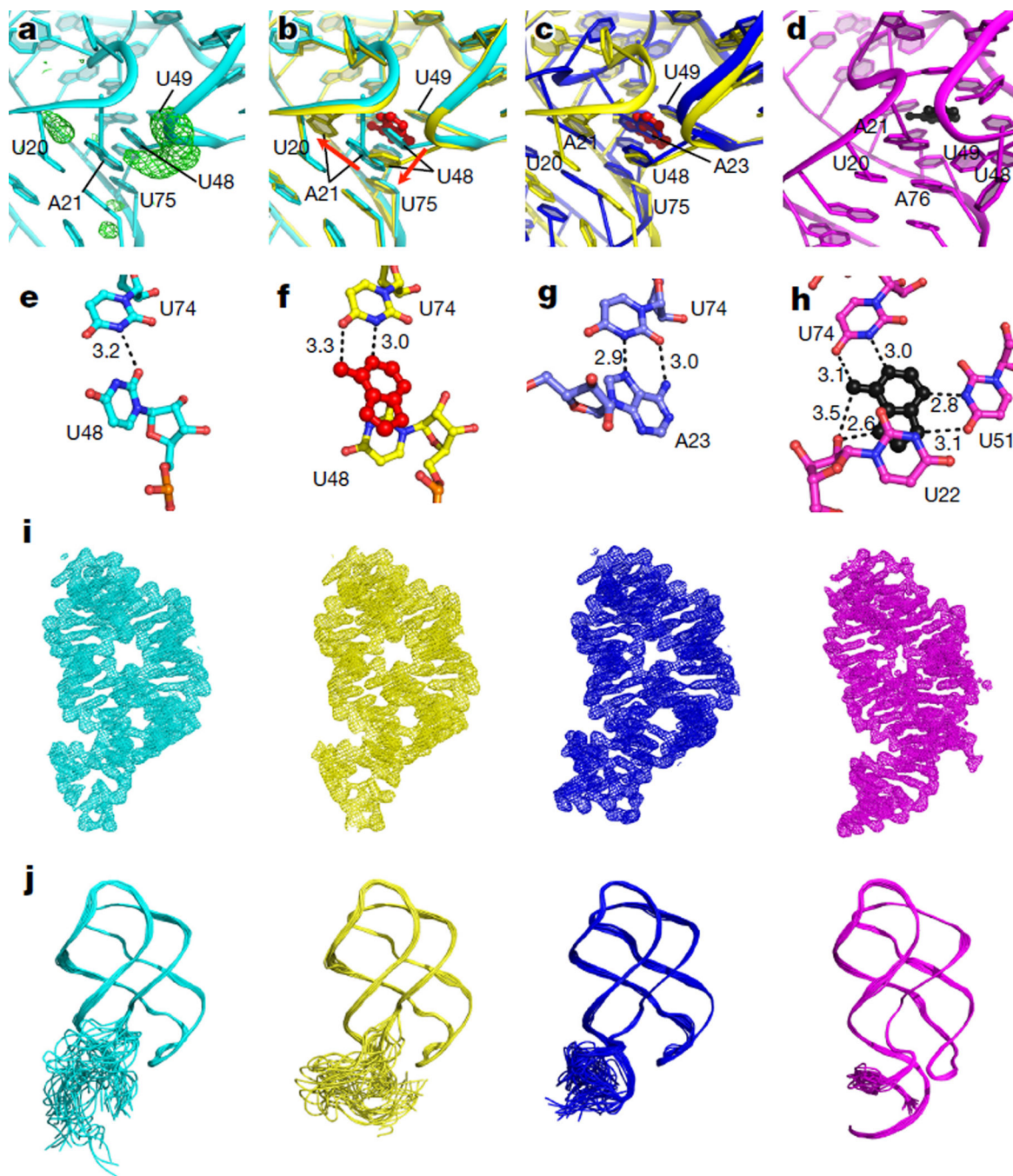


Figure 4. Visualizing the ligand-bound intermediate state

a. $F_o - F_c$ map (3σ , green) of the binding pocket of apo2 (cyan), calculated after refining the apo-rA71 structure against the 10-s-mix data with adenine in the binding pocket and U48 removed, revealing altered conformations for U48 (large peak) and A21 (smaller peak). **b.** Superimposition of apo2 (cyan) and IB (yellow) states, showing the different conformations for U48 and A21. Adenine (red) binding to the apo2 state (cyan) results in displacement of U48, and consequently A21, to form the IB state (yellow). **c.** Superimposition of the apo1 (blue) and IB (yellow) structures, revealing very similar base-stacking interactions, in which

A23 of apo1 (blue) takes the place of the IB ligand (red). **d**, Three-way junction with the adenine ligand (black) of the ligand-bound state (PDB code 4TZX) shown for comparison. **e–h**, Ball-and-stick models, with hydrogen-bond interactions shown, of key residues in the ligand-binding pockets of apo2 (**e**), IB (**f**), apo1 (**g**) and ligand-bound (**h**) states. **i**, $2 F_o - F_c$ electron density maps contoured at 1σ for apo2 (cyan), IB (yellow), apo1 (blue) and ligand-bound (magenta) states. **j**, Structure ensembles of apo2 (cyan), IB (yellow), apo1 (blue) and ligand-bound (magenta) structures from time-averaged molecular dynamics ensemble refinement, demonstrating the flexibility/stability of P1 in each of the four conformations.